ChemPhysMater 4 (2025) 321–329

Contents lists available at ScienceDirect

ChemPhysMater

journal homepage: https://www.keaipublishing.com/en/journals/chemphysmater/

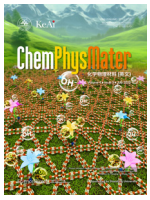

Research Article

Electronic perturbation of Pd single-atom catalysts on graphdiyne derivatives toward effective electrocatalytic nitrate reduction

Cheng Wang[a,b], Tao Song[a,b,c], Hao Dai[a,b], Siyan Shu[a,b], Shenghan Zhang[d], Hongliang Dong[d,e], Yongfei Ji[f,*], Lele Duan[b,g,h,*]

[a] Department of Chemistry, Southern University of Science and Technology, Shenzhen 518055, China
[b] Center of Artificial Photosynthesis for Solar Fuels and Department of Chemistry, Westlake University, Hangzhou 310030, China
[c] School of Chemistry and Chemical Engineering, Harbin Institute of Technology, Harbin 150001, China
[d] Center for High Pressure Science and Technology Advanced Research, Shanghai 201203, China
[e] Shanghai Key Laboratory of Material Frontiers Research in Extreme Environments (MFree), Institute for Shanghai Advanced Research in Physical Sciences (SHARPS), Shanghai 201203, China
[f] School of Chemistry and Chemical Engineering, Guangzhou University, Guangzhou 510006, China
[g] Division of Solar Energy Conversion and Catalysis at Westlake University, Zhejiang Baima Lake Laboratory Co., Ltd., Hangzhou 310000, China
[h] Institute of Natural Sciences, Westlake Institute for Advanced Study, Hangzhou 310024, China

ARTICLE INFO

Keywords:
Electrochemical nitrate reduction
Ammonia synthesis
Single-atom catalyst
Palladium
Graphdiyne

ABSTRACT

Electrocatalytic reduction of nitrate (NO_3^-) to ammonia (NH_3) is a promising approach for addressing water pollution caused by nitrate and producing industrial feedstock NH_3. However, a significant challenge lies in effectively suppressing the formation of undesired byproducts such as H_2, N_2, NO_2^-, and N_2H_4. In this study, three Pd single-atom catalysts (SACs) supported on graphdiyne (GDY) derivatives functionalized with electron-withdrawing and electron-donating groups denoted as Pd/GDY-F, Pd/GDY-H and Pd/GDY-OMe were prepared. Structural characterization showed that due to the electron induction effect of the functional groups, Pd/GDY-F displays the highest Pd valence state, followed by Pd/GDY-H and Pd/GDY-OMe. Interestingly, the nitrate reduction activity also follows the order Pd/GDY-F > Pd/GDY-H > Pd/GDY-OMe, indicating that the nitrate reduction activity of Pd depends on the Pd oxidation state. In addition, the anion exchange ionomers and high nitrate concentrations are beneficial for nitrate reduction. Under optimized conditions, Pd/GDY-F displays a high Faraday efficiency (FE) of 96.2% ± 2.5% toward NH_3. Mechanistic studies revealed that high-valence Pd atoms favor the adsorption of nitrate reduction intermediates, leading to a high Faraday efficiency for NH_3.

1. Introduction

The excessive use of nitrogen fertilizer and discharge of large amounts of domestic sewage and industrial wastewater have resulted in the significant presence of NO_3^- in wastewater and groundwater. Electrocatalytic NO_3^- reduction (NO_3RR) to NH_3 has emerged as an environmentally friendly approach to address NO_3^- pollution [1,2]. However, during the reduction process from NO_3^- to NH_3, the valence of N is reduced from +5 to −3, involving the participation of a total of 8 electrons and 9 protons [3], which leads to the formation of various intermediates throughout the reaction process [4,5]. The production of multiple intermediates may give rise to the formation of by-products such as NO_2^-, N_2H_4, and N_2 [6]. Additionally, the Faradaic efficiency (FE) for this process is also affected by the competing hydrogen evolution reaction (HER). While *H participates in the reduction process of NO_3^-, excessive *H or its reaction with protons generates H_2 as a by-product. Therefore, it is necessary to balance the *H generation rate to inhibit HER while enhancing NH_3 selectivity [7,8]. Achievement of simultaneous reduction in the HER rate and inhibition of by-product formation poses a significant challenge in electrocatalytic NH_3 synthesis via NO_3RR. In catalysis, regulation of the electronic structure at active centers is a viable method for improving catalyst performance [9]. Similarly, in NH_3 synthesis via NO_3RR, the electronic structure at the active sites can be regulated to promote intermediate adsorption while inhibiting HER progress, resulting in enhanced catalytic activity and selectivity [10,11].

An increasing number of high-performance catalysts have been developed by manipulating the electronic structure of the active center to enhance catalytic activity [12]. For instance, the doping of B atoms into a Cu-based catalyst increases the valence state of the local Cu sites, thereby achieving higher NH_3 selectivity [13]. The construction of Cu-Pd bimetallic sites involves the introduction of Pd onto the surface of

* Corresponding authors.
E-mail addresses: yongfeiji2018@gzhu.edu.cn (Y. Ji), duanlele@westlake.edu.cn (L. Duan).

https://doi.org/10.1016/j.chphma.2025.02.005
Received 30 October 2024; Received in revised form 11 January 2025; Accepted 19 February 2025
Available online 16 March 2025

the Cu metal, enabling the regulation of the electronic structure at the catalytic active center, and resulting in an alloy catalyst with superior catalytic activity [14]. For such Cu-Pd catalysts, the oxidation states of the metal active centers can be regulated by creating diverse coordination environments, obtaining molecular catalysts with varying catalytic activities [15]. Single-atom catalysts (SACs) have attracted significant attention in various catalytic fields because of their advantage of ultra-high atomic utilization [16–18]. In the NO_3RR used for the production of NH_3, the atomically dispersed active sites can impede $^*N$ coupling and inhibit N_2 formation [19,20]. Furthermore, modifying the coordination environment of SACs allows for the regulation of the electronic structure at the active center, influences the adsorption of the intermediates, and improves NH_3 selectivity [21,22]. Liu's group successfully doped halogen elements (Cl) into a Pd SAC supported on Cu_2O to control the electronic structure of the Pd 3d orbital. This modification enhanced the $^*H$ generation rate under high-pH conditions and enabled a high FE of NH_3 at a current density of 2.0 A cm^{-2} [23].

As a precious metal, Pd shows excellent corrosion resistance (which is highly important in sewage treatment), but also good hydrogen evolution activity [24,25], mainly because its d orbital can interact with the s orbital of $^*H$ to form a strong Pd–H bond [23]. However, atomically dispersed Pd can effectively reduce the coupling of $^*H$ and decrease the generation of H_2. Therefore, it is possible to achieve equilibrium between the production and consumption of $^*H$ in the NO_3RR by regulating the electronic structure of the Pd atoms [26,27]. Graphdiyne (GDY) is a novel two-dimensional carbon nanomaterial composed of sp- and sp^2-hybridized carbon atoms that was first synthesized by the Li group in 2010 [28]. The porous structure and coordinating C≡C triple bonds of GDY make it an ideal substrate for attaching metal atoms [29–31]. Additionally, different functional groups can be introduced into GDY to modulate the electronic structure of the attached single atoms (SAs) [32]. Moreover, stable d–π interaction can be formed between Pd and C≡C triple bond in GDY, which prevents the aggregation of Pd SAs [33]. Therefore, the use of various functional groups to regulate the electronic structure of GDY-supported Pd SAs is a feasible approach for the modification of their performance in NO_3RR to NH_3. In this study, different electron-withdrawing and electron-donating groups (–F, –H, and –OMe) were introduced into GDY to alter the electron density of the conjugated π system, obtaining Pd SACs (Pd/GDY-F, Pd/GDY-H and Pd/GDY-OMe) with distinct oxidation states. The structure-activity relationship governing the NO_3RR to NH_3 was investigated by regulating the electronic structure of the Pd SAs. Through structural characterization, the order of the Pd valence in the three catalysts was determined to be Pd/GDY-F > Pd/GDY-H > Pd/GDY-OMe. The FE toward NH_3 of Pd/GDY-F was approximately three times higher than that of Pd/GDY-OMe under similar conditions, suggesting that the high-valence Pd SA exhibited superior catalytic activity and selectivity. This finding demonstrates the successful regulation of the electronic structure and catalytic activity of Pd using a molecular engineering strategy. The catalytic properties of Pd/GDY-F were optimized by changing the ion-exchange ionomers and varying the reaction time and NO_3^- concentration. Under optimized conditions, Pd/GDY-F displayed a high FE of 96.2% ± 2.5% toward NH_3 at −0.7 V. The reaction mechanism was investigated using in situ infrared spectroelectrochemistry and density functional theory calculations. To the best of our knowledge, few studies have focused on the structure-activity relationship for the regulation of the electronic structure of SAs supported by GDY and its effect on NO_3RR to NH_3. The electronic structure perturbation strategy used in this study is effective for single-atom catalysts and can be used to investigate the effects of electronic structure modification for other metal SACs used as catalysts for various chemical reactions.

2. Results and discussion

2.1. Material synthesis and characterization

The synthetic routes for Pd/GDY-R materials are shown in Fig. 1. First, 3, 6-substituted 1, 2, 4, 5-tetrakis((trimethylsilyl)ethynyl)benzene molecules (**1a–c**; Fig. 1) with different electron-withdrawing and electron-donating groups, such as –F, –H, and –OMe, were synthesized according to the reported methods (see more details in the Supporting Information and Figs. S1–S3). As shown in Fig. 1, deprotection of the trimethylsilyl groups from the above precursors by fluoride yields 1, 2, 4, 5-tetraethynyl-3, 6-difluorobenzene (**2a**), 1, 2, 4, 5-tetraethynylbenzene (**2b**), and 1, 2, 4, 5-tetraethynyl-3, 6-dimethoxybenzene (**2c**), respectively. Then, the copper-ion-catalyzed Eglinton reaction was used to synthesize GDY derivatives according to the reported method [34], yielding GDY-R (R = –F, –H, and –OMe; their characteristics are in line with previous reports, but are not discussed herein as they are known materials). With these three materials in hand, GDY-R-supported Pd SACs (Pd/GDY-R; see their chemical structures in Figs. 2(a)(e)(i) were prepared by mixing GDY-R and K_2PdCl_4 in DMF at low temperature (0 °C) according to the procedure reported by the Lu group [35]. The contents of Pd in the three catalysts, detected by the inductively coupled plasma mass spectrometry (ICP-MS), are close to each other with 0.18 wt% for Pd/GDY-F, 0.19 wt% for Pd/GDY-H, and 0.22 wt% for Pd/GDY-OMe. The morphology of Pd/GDY-R was characterized by transmission electron microscopy (TEM). The TEM images of Pd/GDY-R show that these catalysts exhibit a typical layered morphology (Figs. S4(a)(c)(e)). Moreover, no metal nanoparticles were observed in the high-resolution transmission electron microscopy (HR-TEM) images (Figs. S4(b)(d)(f)). The atomic dispersion of Pd on the GDY-R supporting material was verified by aberration-corrected high-angle annular dark-field scanning transmission electron microscopy (AC-HAADF-STEM). As shown in Figs. 2(b)(c)(f)(g)(j)(k), a large number of isolated bright dots can be observed in the images at both 5 nm and 2 nm scales, with no apparent nanoparticles or nanoclusters. Additionally, energy-dispersive spectroscopy (EDS) mapping images revealed uniformly dispersed C and Pd in all three Pd/GDY-R materials while the F element is present solely in Pd/GDY-F (Figs. 2(d)(h)(l)). In addition, contact angle measurements (Fig. S5) show that their contact angles are between 117.80° and 131.30°; such small differences in contact angles indicate that the catalytic properties of these three materials are not drastically affected by the differences in hydrophobicity.

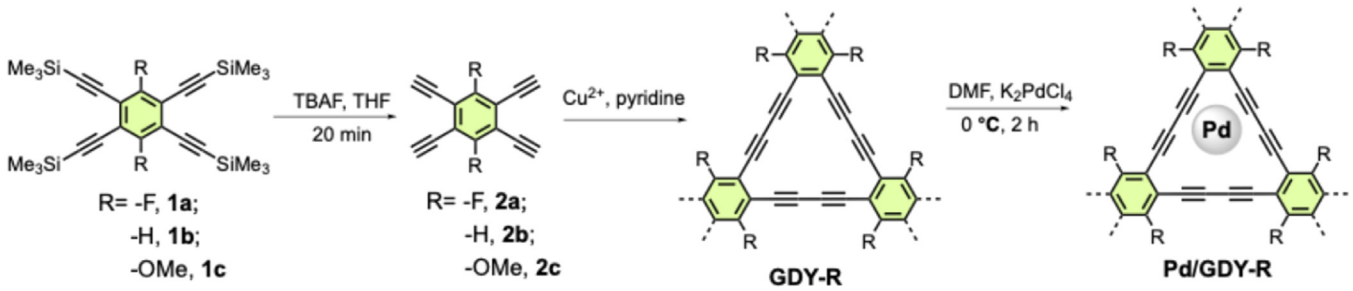

Fig. 1. Synthetic routes for Pd/GDY-R (R = –F, –H, –OMe).

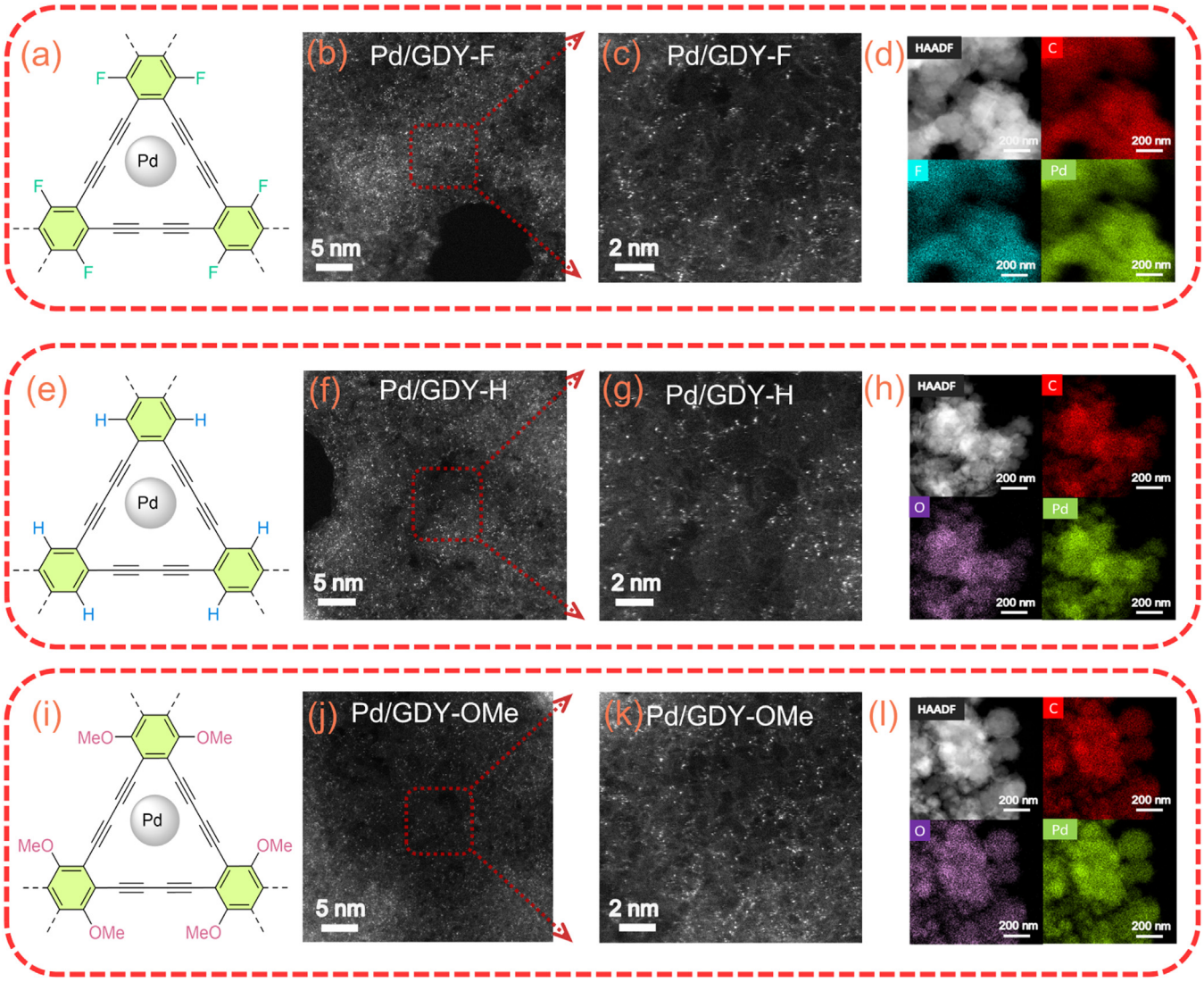

Fig. 2. Chemical structures of catalysts (a) Pd/GDY-F, (e) Pd/GDY-H and (i) Pd/GDY-OMe. AC-HAADF-STEM images of (b)(c) Pd/GDY-F, (f)(g) Pd/GDY-H and (j)(k) Pd/GDY-OMe. Corresponding EDS mapping images of (d) Pd/GDY-F, (h) Pd/GDY-H and (l) Pd/GDY-OMe.

The catalysts were characterized by X-ray diffraction (XRD), Raman spectroscopy, Fourier-transform infrared spectroscopy (FTIR), and X-ray photoelectron spectroscopy (XPS). From the results of XRD analysis (Fig. S6(a)), it is observed that there were no characteristic sharp diffraction peaks of crystalline metals, and only a wide peak at 21° was observed for all three catalysts. Therefore, there was no metal aggregation in the materials, which is in good agreement with the electron microscopy results. The Raman spectra (Fig. S6(b)) clearly reveal the D band at 1356 cm^{-1} and the G band at 1576 cm^{-1}. The D and G bands were assigned to the vibrations of sp^2-hybridized disordered carbon and ordered graphitic carbon, respectively. Weak peaks at 2180 and 2250 cm^{-1} caused by the oscillation of the diacetylene bond were also observed [36]. In their FTIR spectra (Fig. S6(c)), the stretching vibration peaks of C–F of Pd/GDY-F and C–OMe of Pd/GDY-OMe were observed near 900 and 1000 cm^{-1}, respectively. The C and O ratios revealed by the XPS data were consistent with the EDS data (Figs. S7), where Pd/GDY-OMe displayed a higher O content than Pd/GDY-F and Pd/GDY-H (Figs. S7(a)(c)). In the high-resolution C 1s XPS spectra (Fig. S7(b)), the peaks of C≡C(sp) and C=C(sp^2) were observed for all three catalysts, while C–F and C–C(sp^3) signals were found for Pd/GDY-F and Pd/GDY-OMe, respectively. Further XPS analysis (Figs. 3(a)–(c)) reveals that the binding energies of Pd are clearly different for all three Pd/GDY-R catalysts. The binding energy values of Pd $3d_{3/2}$ ($3d_{5/2}$) are 342.6 eV (337.34 eV) for Pd/GDY-F, 342.38 eV (337.12 eV) for Pd/GDY-H, and 342.21 eV (336.95 eV) for Pd/GDY-OMe, respectively. As expected, the Pd binding energy displayed a decreasing trend due to the electronic induction effect of the functional groups, indicating that the valence state of Pd was decreased by changing the R groups from –F to –H and further to –OMe. Therefore, electronic perturbation of the GDY-supported Pd SACs was successfully achieved by introducing different electron-donating and -withdrawing groups.

The electronic structure and coordination environment of the Pd SAs on GDY-R were further characterized by X-ray absorption spectroscopy (XAS). Fig. 3(d) shows the K-edge X-ray absorption near-edge structure (XANES) spectra of Pd for a series of Pd-containing materials including Pd foil, PdO, and Pd/GDY-R. The near-edge positions of Pd/GDY-R are between those of the Pd foil and PdO, indicating that the Pd valence state of Pd/GDY-R is between 0 and 2 [33]. Moreover, the Pd valence states are in the order Pd/GDY-F > Pd/GDY-H > Pd/GDY-OMe, and the electron-withdrawing group shifts the Pd valence state in the positive direction, which is consistent with the XPS results mentioned above. In the Fourier-transformed k^2-weighted extended X-ray absorption fine structure (FT-EXAFS) spectra (Fig. 3(e)), a clear peak at approximately 2.4 Å appears in Pd foil, which is assigned to the Pd–Pd bond [37].

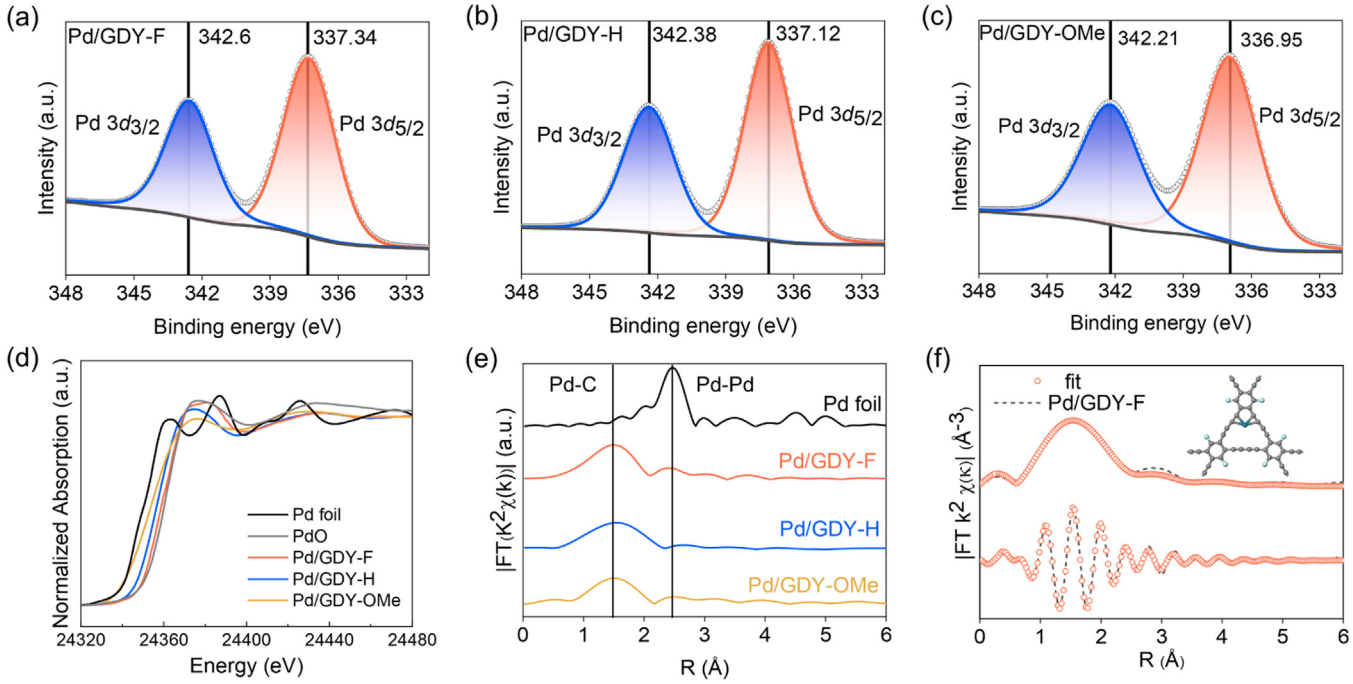

Fig. 3. High-resolution XPS Pd 3d spectra of (a) Pd/GDY-F, (b) Pd/GDY-H and (c) Pd/GDY-OMe. (d) Pd K-edge XANES spectra of the prepared Pd/GDY-R with Pd foil and PdO. (e) Fourier transformation k^2-weighted EXAFS spectra in R space. (f) First-shell (Pd−C) fitting of Fourier transformations of EXAFS spectra for Pd/GDY-F. The top and bottom traces show the real and imaginary parts, respectively. (The inset shows the atomic structure model of Pd/GDY-F).

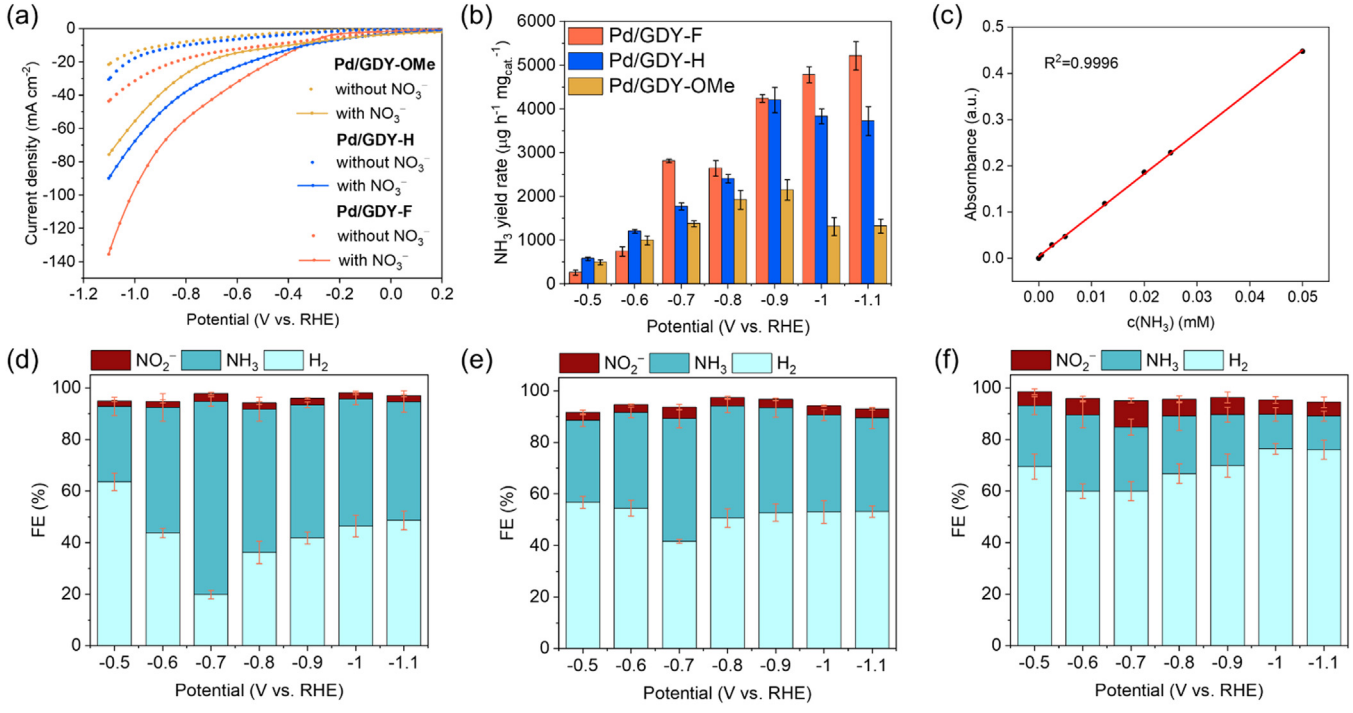

Fig. 4. Electrocatalytic performance of NO_3RR. (a) LSV curves of Pd/GDY-R in the Ar-saturated 0.1 M KOH with and without 0.1 M KNO_3 electrolyte. (b) Rate of NH_3 production in the NO_3RR for Pd/GDY-R. (c) Corresponding calibration curve for NH_3. FEs of all products on (d) Pd/GDY-F, (e) Pd/GDY-H and (f) Pd/GDY-OMe in the NO_3RR experiments.

For Pd/GDY-R, a major signal peak at approximately 1.5 Å appears for each sample, which was assigned to the Pd−C bond, whereas the Pd-Pd scattering signal was not observed [38]. In addition, wavelet transform (WT) was used to probe the Pd K-edge EXAFS oscillations (Fig. S8), and the WT-EXAFS contour plots show one intensity maximum at ~5 $Å^{-1}$, due to the Pd−C scattering path. Furthermore, the proposed chemical structures of Pd/GDY-R were optimized using density functional theory (DFT) and then used for quantitative EXAFS fitting. The fitting results show that the Pd atom of Pd/GDY-R is coordinated to four C atoms (Figs. 3(f) and S9, Table S1), similar to the structure proposed for Pd/GDY by the Lu group [35]. The XAS data further demonstrate that Pd was atomically dispersed over GDY-R, and that its electronic structure was

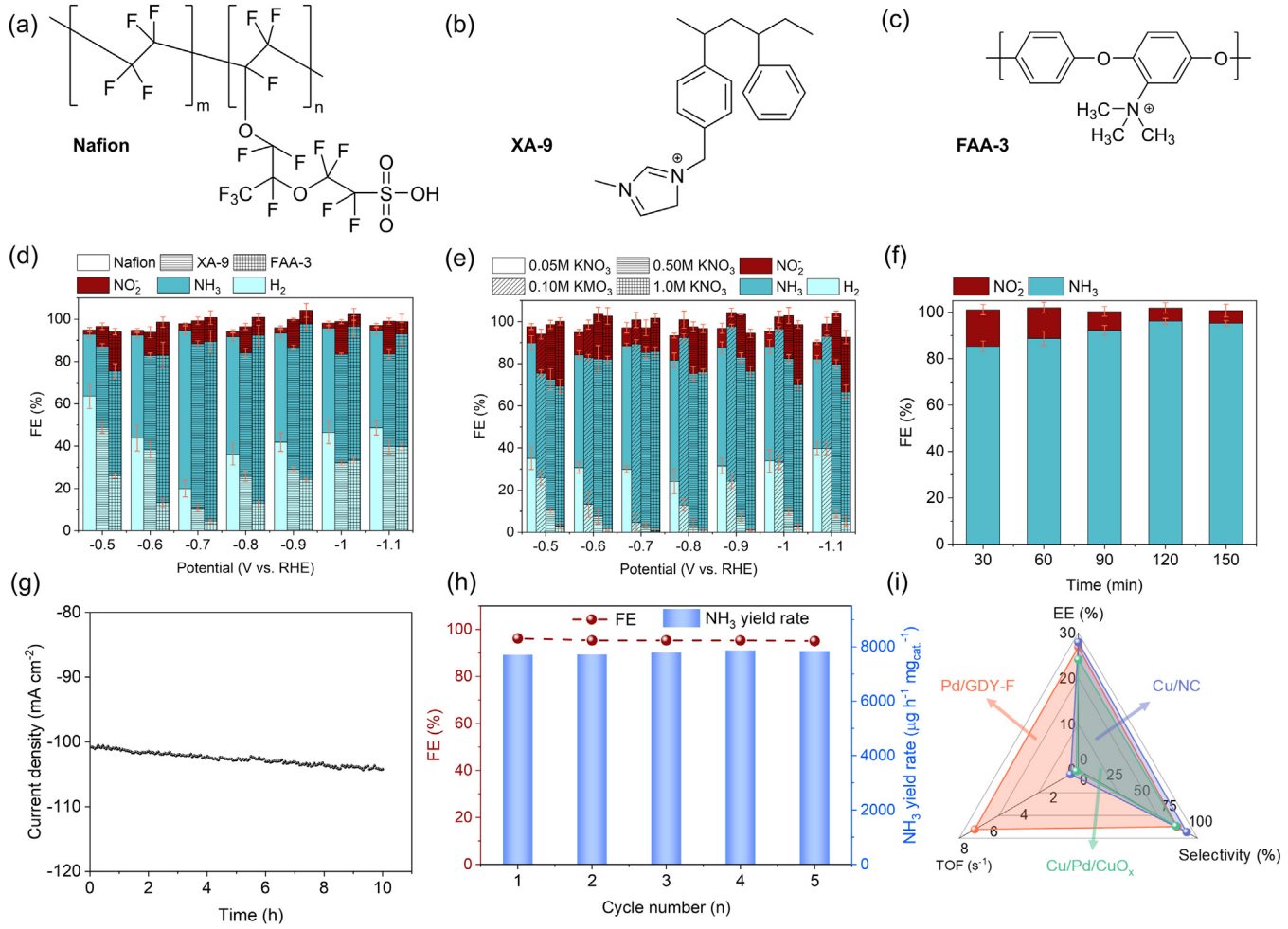

Fig. 5. Chemical structures of ionomers (a) Nafion, (b) FAA-3 and (c) XA-9. (d) FEs of total products under different ion exchange solutions. (e) FEs of total products at different concentrations of KNO_3. (f) FEs of total products at different sampling time. (g) Chronoamperometry curve of Pd/GDY-F via 10 h electrolysis at −0.7 V. (h) Rate of NH_3 production and FE of Pd/GDY-F obtained for five cycle tests. (i) Comparison of catalytic performance between Pd/GDY-F and other catalysts.

regulated by introducing electron-withdrawing and -donating groups on the GDY skeleton.

2.2. *Electrochemical NO_3RR*

The fine-tuned electronic structures of Pd/GDY-R provide good model catalysts to reveal the structure-activity relationship of Pd SAs toward the NO_3RR. Therefore, the electrochemical NO_3RR using Pd/GDY-R was carried out in an H-type electrochemical cell, with a catalyst-modified carbon paper as the working electrode, an Ag/AgCl (filled with saturated KCl electrolyte) electrode as the reference electrode, and a Pt foil as the counter electrode. The electrolyte employed for the electrocatalysis was a mixed aqueous solution of KOH (0.1 M KOH and 100 mM KNO_3. The main byproducts (H_2 and NO_2^-) and target product (NH_3) of the NO_3RR were analyzed by gas chromatography and the colorimetric method, respectively. The results are shown in Fig. 4 and the standard calibration curves are shown in Fig. 4(c) and Figs. S10–S12. All potentials reported herein are relative to the reversible hydrogen electrode (RHE).

Linear sweep voltammetry (LSV; Fig. 4(a)) was applied to Pd/GDY-R in an Ar-saturated 0.1 M KOH solution with and without 100 mM KNO_3. Compared to the electrolyte without KNO_3, the current density of all three catalysts increased in the presence of KNO_3, indicating the occurrence of NO_3RR. Notably, Pd/GDY-F exhibited a more favorable onset potential and a higher current density than the other two catalysts, suggesting good reactivity toward NO_3^-. To further assess the catalytic performance, potentiostatic electrolysis was conducted over a potential range of −0.5 to −1.1 V, and the reaction products along with the corresponding FEs were recorded. Among the three catalysts, Pd/GDY-F demonstrates the best catalytic performance, achieving the highest FE (74.9% ± 1.8%) at −0.7 V, with an NH_3 synthesis rate of 2812.8 ± 40.8 μg h^{-1} $mg_{cat.}^{-1}$ (Fig. 4(b)). At this potential, the FE was approximately 1.5 times that of Pd/GDY-H and three times that of Pd/GDY-OMe (Figs. 4(d)–(f)). Moreover, Pd/GDY-F significantly outperformed the other two catalysts in suppressing HER, with the most pronounced inhibition observed at −0.7 V. These findings suggest that the presence of high-valence Pd in Pd/GDY-F can effectively reduce H_2 generation and enhance the selectivity and catalytic activity toward NH_3 synthesis. Additionally, the double-layer capacitance (C_{dl}) values for Pd/GDY-F, Pd/GDY-H, and Pd/GDY-OMe are measured to be 9.26, 9.12, and 8.82 mF cm^{-2}, respectively, indicating that their electrochemical active surface areas (ECSA) are nearly identical (Fig. S13).

Subsequently, a systematic comparative study on the performance of Pd/GDY-F was conducted using different ion-exchange ionomers, varying concentrations of the KNO_3 electrolyte, and controlling electrolysis duration. First, we assessed the performance differences by preparing working electrodes using different ion-exchange ionomers, such as the cation-exchange ionomer Nafion and two anion-exchange ionomers, XA-9 and FAA-3 (Figs. 5(a)–(c)). As shown in Fig. 5(d), compared to the Nafion ionomer, the electrodes prepared with anion-exchange ionomers

exhibited higher FE for NH_3 and lower FE for H_2. At a potential of −0.7 V, the FEs of the electrodes with the two anion exchange ionomers reached 77.5% ± 1.4% and 84.8% ± 5.2%, respectively, while the NO_2^- selectivity increased significantly, from 3.0% ± 0.5% to 10.9% ± 1.8% and 11.4% ± 3.2%. The observed phenomena were most likely due to the cationic head groups of the anion exchange ionomers attracting NO_3^- anions, increasing the surface NO_3^- concentration, and thus improving the NH_3 production rate of NO_3RR. Next, using the best-performing anion exchange ionomer, FAA-3, we explored the catalytic performance of Pd/GDY-F at different KNO_3 concentrations. As illustrated in Fig. 5(e), increasing KNO_3 concentration enhances the NO_3RR. The NH_3/NO_2^- FEs at −0.7 V were 58.6% ± 1.3%/8.5% ± 2.5%, 84.8% ± 2.0%/11.4% ± 3.6%, 82.1% ± 2.9%/11.8% ± 3.7% and 85.3% ± 2.2%/15.8% ± 2.1% for 0.05, 0.10, 0.50, and 1.00 M KNO_3, respectively. Moreover, the FE of H_2 decreased significantly with increasing concentration and was almost completely suppressed at the highest KNO_3 concentration (1.0 M). These results indicate that Pd/GDY-F shows better performance at high KNO_3 concentrations. Based on the optimal KNO_3 concentration, the product distribution was monitored as a function of electrolysis time at −0.7 V. As shown in Fig. 5(f), with increasing electrolysis duration, the FE for NH_3 gradually increased while that for NO_2^- decreased. The FE for NH_3 reached a maximum of 96.2% ± 2.5% at 120 min and remained relatively stable at 150 min (95.3% ± 1.2%).

Potentiostatic electrolysis and cycle tests (Figs. 5(g)(h)) were carried out under the following conditions: Pd/GDY-F as the catalyst, −0.7 V as the applied potential, FAA-3 as the anion exchange membrane, 1.0 M KNO_3 aqueous solution as the electrolyte, and 120 min for each run. Five experiments repeated over 10 h showed that the current density remained stable. In addition, the FE and synthesis rate of NH_3 remained unchanged during the cycle tests, indicating the good stability of Pd/GDY-F in NO_3RR. The catalyst was characterized using AC-HAADF-STEM after potentiostatic testing (Fig. S14), and many bright spots were observed, indicating that the Pd SAs did not agglomerate, which is consistent with the EDS mapping images showing well-dispersed elements. Fig. 5(i) compares Pd/GDY-F with other catalysts in terms of energy efficiency (EE), turnover frequency (TOF), and selectivity toward NH_3. While Pd/GDY-F shows only slight differences in EE (26.91%) and selectivity (91.25%) from other catalysts, its TOF (6.96 s^{-1}) is significantly better than those of the other catalysts. Table S2 compares Pd/GDY-F and other catalysts in terms of the FE and yield rate toward NH_3. The results showed that Pd/GDY-F is a state-of-the-art catalyst for NO_3RR.

To further investigate the impact of electronic structure modulation of the Pd SAs on catalytic reactivity and product selectivity, in situ attenuated total reflection surface-enhanced infrared absorption spectroscopy (ATR-SEIRAS) was employed for all three catalysts. The ATR-SEIRAS experiments were conducted in an Ar-saturated electrolyte containing 0.1 M KOH and 0.1 M KNO_3, using an H-type cell. The potential sweep was carried out from −0.1 to −1.1 V, where several specific signals were detected (Figs. 6(a)–(c)). The upward peak at 1210 cm^{-1} corresponds to the formation of the $^*NO_2$ intermediate, while the downward peak at 1640 cm^{-1} arises from the H–O–H vibration during the decomposition of H_2O [39]. Two key intermediate signals, $^*NH$ (~1515 cm^{-1}) and $^*NH_3$ (~1460 cm^{-1}), were identified for both Pd/GDY-F and Pd/GDY-H [20,40]. As the reduction potential increased, the intensity of the signal peaks in Pd/GDY-F becomes stronger compared to Pd/GDY-H, while Pd/GDY-OMe showed a weaker $^*NH$ signal. These results indicate that Pd/GDY-F exhibits stronger adsorption capacity for the reaction intermediates, which enhances its selectivity toward NH_3 production.

Finally, DFT calculations were conducted to further investigate the experimental results. Bader charge calculations revealed that the Pd centers in Pd/GDY-F, Pd/GDY-H, and Pd/GDY-OMe were positively charged by 0.30, 0.26, and 0.25 e respectively, consistent with the EXAFS spectra [41]. While the differences in the Bader charges were subtle, Fig. 7(a) highlights significant variations in the projected density of states (PDOS) of Pd, which can influence its interactions with adsor-

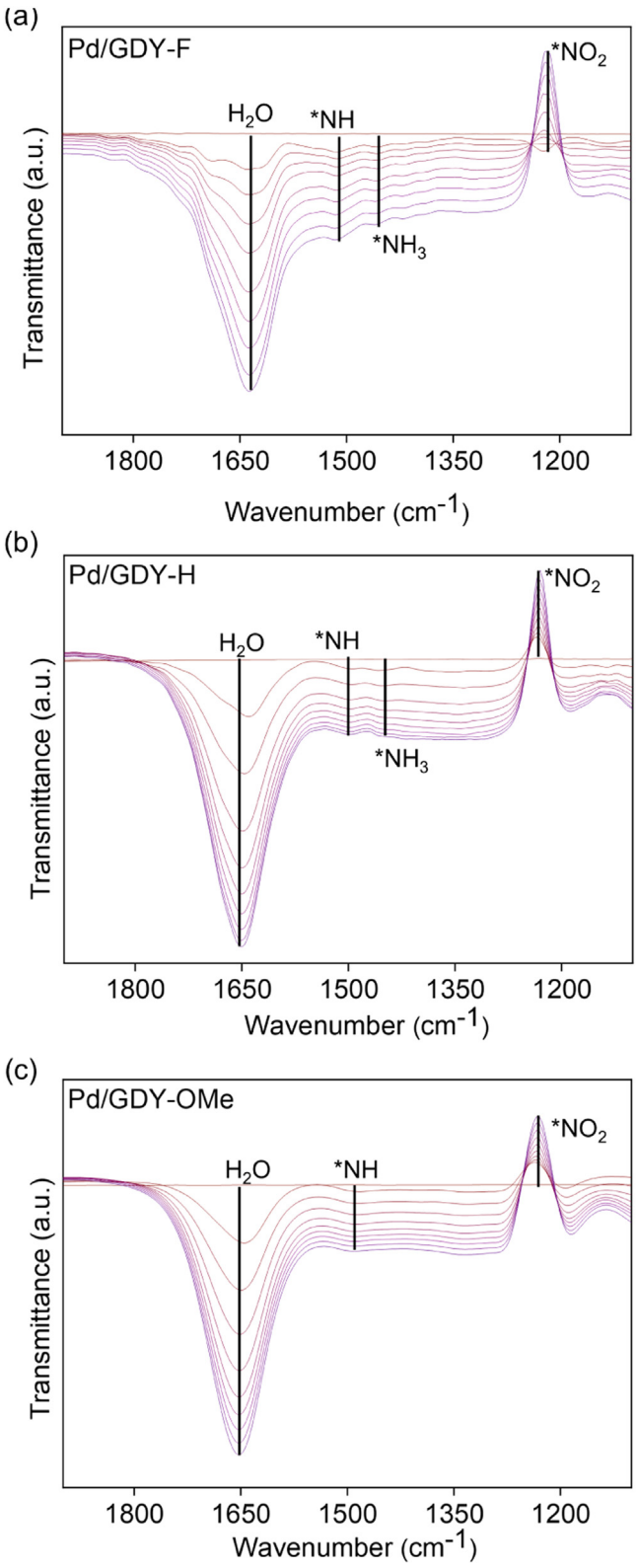

Fig. 6. In situ ATR-SEIRAS spectra of (a) Pd/GDY-F, (b) Pd/GDY-H and (c) Pd/GDY-OMe recorded at a potential range from −0.1 to −1.1 V.

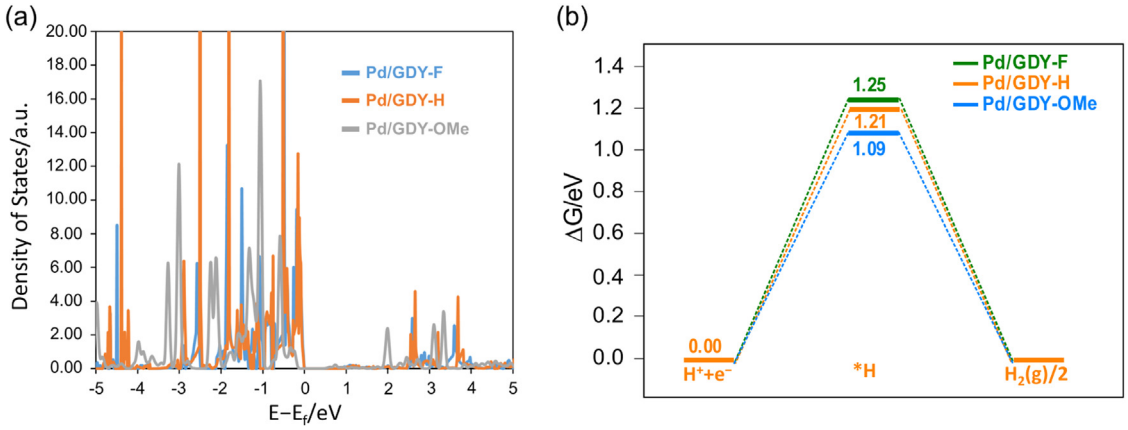

Fig. 7. (a) Projected density of states of Pd in three graphdiyne derivatives. (b) Free energy surface for the hydrogen evolution reaction.

bates. The adsorption energy of NO_3^- was calculated as −0.62, −0.52, and −0.58 eV on Pd/GDY-H, Pd/GDY-F, and Pd/GDY-OMe, respectively, suggesting that F and OMe substitution promotes nitrate adsorption. The trend of NO_3^- adsorption energy does not follow that of the Bader charge of Pd, likely due to the influence of the detailed electronic structure of the Pd centers. Furthermore, the binding strength of *H was the strongest for Pd/GDY-OMe and weakest for Pd/GDY-F (Fig. 7(b)), suggesting that Pd/GDY-F can more effectively suppress the HER, which is consistent with the experimental findings.

The free-energy surfaces (FES) are shown in Fig. S15. The optimized structures of the intermediates are summarized in Fig. S16. The binding free energies of the intermediates of the three derivatives are relatively similar. Generally, the intermediates bind most strongly to Pd/GDY-OMe and show the weakest binding for Pd/GDY-F, likely due to the electrophilic nature of the intermediates. The potential-limiting step is identified as the reduction of *NO to *NHO, with limiting potentials (U_L) of −0.11, −0.05, and 0.01 V for Pd/GDY-F, Pd/GDY-H, and Pd/GDY-OMe, respectively. Although this trend does not align with the experimentally observed activity, the small U_L values suggest that other reaction steps may also be rate-limiting and that kinetic effects should be considered. For instance, although *NH is thermodynamically less favorable than *NH_2OH based on FES, *NH was observed in the ATR-SEIRAS spectra, suggesting that the reduction of *NHOH to *NH may be kinetically preferred. Additionally, *NO_2 appeared as an intermediate, and the trend in the reaction energies for its reduction are consistent with the experimental activity observations. However, *NH was thermodynamically less favorable than *NH_2OH based on the FES, and *NH was observed in the ATR-SEIRAS spectra, suggesting that the reduction of *NHOH to *NH may be kinetically preferred. However, calculations of kinetic barriers for the proton-coupled electron transfer steps remain challenging [42]. In addition, the differences in energetics were comparable to the typical error margins in DFT calculations; therefore, kinetic barriers were not determined in this study.

3. Conclusion

In summary, three Pd SACs, Pd/GDY-F, Pd/GDY-H, and Pd/GDY-OMe, were synthesized and their Pd valence states were regulated by introducing different electron-withdrawing and -donating groups (–F, –H, and –OMe) onto the supporting graphdiyne materials. The electronic structure regulation and structure-activity relationships of Pd/GDY-R toward NO_3RR were systematically studied. Structural characterization revealed that the valence state of Pd in the catalysts followed the order Pd/GDY-F > Pd/GDY-H > Pd/GDY-OMe. In the subsequent performance evaluation, Pd/GDY-F exhibited the highest FE for NH_3 production, reaching 74.9% ± 1.8% at −0.7 V with 0.1 M KOH and 0.1 M KNO_3 as the electrolyte, which is approximately three times that of Pd/GDY-OMe under the same conditions. The NH_3 production rate of Pd/GDY-F was 2812.8 ± 40.8 μg h^{-1} $mg_{cat.}^{-1}$. These results demonstrate that higher-valence Pd SACs possess enhanced catalytic activity and selectivity for NO_3RR. Further exploration of Pd/GDY-F under different conditions, such as by varying the ion exchange ionomers, NO_3^- concentration, and reaction time, revealed that the highest performance was achieved using the FAA-3 anion exchange ionomer in a highly concentrated NO_3^- electrolyte, with optimal results (96.2% ± 2.5% FE) observed after 120 min of reaction time. In-situ ATR-SEIRAS experiments provided insights into the reaction mechanism, showing that Pd/GDY-F exhibited stronger adsorption of reaction intermediates, which improved NH_3 selectivity. Finally, we found positive charges for the Pd centers of the three catalysts by DFT calculations, in good agreement with the EXAFS results. Pd/GDY-F inhibits HER much more strongly than the other two catalysts. Our work demonstrates a feasible approach for preparing SACs with varying metal electronic structures, and these SACs serve as model catalysts to investigate the relationship between the metal electronic structure and the catalytic performance in various reactions beyond NO_3RR.

4. Outlook

To address the water pollution caused by NO_3^-, a variety of treatment methods have emerged, such as physical adsorption, biochemical processing, and chemical transformation. Among these, the chemical transformation method has many advantages, such as high selectivity, low cost, and safety [43]. As a form of chemical transformation, NO_3RR has broad application prospects. To date, while a wide variety of high-performance catalysts with a variety of structures have been investigated [44–46], maintaining high selectivity at low concentrations (50 mg N/L) is still challenging [47]. Wang's al. realized the transformation of industrial wastewater (2000 ppm) into drinking water (<50 ppm) under an industrial current and maintained an FE of >90% toward NH_3 using Ru-Cu NWs as the catalyst [48]. The successful catalyst promoted the application of NO_3RR in wastewater treatment at the industrial level. Nevertheless, to truly promote its commercial use, it is still necessary to overcome the technical barriers between basic research and practical applications. This requires combined expertise in environmental technology, electrochemistry, chemical engineering, and chemical economics [49].

Declaration of Competing Interest

The authors declare the following personal relationships which may be considered as competing interests: Lele Duan is currently employed by Zhejiang Baima Lake Laboratory Co., Ltd. Other authors declare that there are no competing interests.

CRediT authorship contribution statement

Cheng Wang: Writing – original draft, Methodology, Investigation. **Tao Song:** Validation, Formal analysis. **Hao Dai:** Investigation. **Siyan Shu:** Investigation. **Shenghan Zhang:** Investigation. **Hongliang Dong:** Investigation. **Yongfei Ji:** Funding acquisition, Investigation, Writing – original draft. **Lele Duan:** Writing – review & editing, Supervision, Funding acquisition, Conceptualization.

Acknowledgements

This work was supported by the National Natural Science Foundation of China (22179057, L.D.), start-up package from Westlake University (L.D.), and Natural Science Foundation of Guangdong Province (2023A1515012238). The authors acknowledge the financial support from the Shanghai Key Laboratory of Material Frontiers Research in Extreme Environments (MFree), China (No. 22dz2260800). We acknowledge support from the BL11B and BL13SSW stations at the Shanghai Synchrotron Radiation Facility (SSRF).

Supplementary materials

Supplementary material associated with this article can be found, in the online version, at doi:10.1016/j.chphma.2025.02.005.

References

[1] Y. Xu, C. Cheng, J. Zhu, B. Zhang, Y. Wang, Y. Yu, Sulphur-boosted active hydrogen on copper for enhanced electrocatalytic nitrate-to-ammonia selectivity, Angew. Chem. Int. Ed. 63 (2024) e202400289, doi:10.1002/anie.202400289.

[2] T. Ren, Z. Yu, H. Yu, K. Deng, Z. Wang, X. Li, H. Wang, L. Wang, Y. Xu, Interfacial polarization in metal-organic framework reconstructed Cu/Pd/CuO_x multi-phase heterostructures for electrocatalytic nitrate reduction to ammonia, J. Appl. Catal. B: Environ. 318 (2022) 121805, doi:10.1016/j.apcatb.2022.121805.

[3] Y. Lou, Q. Zheng, S. Zhou, J. Fang, O. Akdim, X. Ding, R. Oh, G. Park, X. Huang, S. Sun, Phase-dependent electrocatalytic nitrate reduction to ammonia on Janus Cu@Ni tandem catalyst, ACS Catal. 14 (2024) 5098–5108, doi:10.1021/acscatal.4c00479.

[4] X. Lu, H. Song, J. Cai, S. Lu, Recent development of electrochemical nitrate reduction to ammonia: A mini review, J. Electrochem. Commun. 129 (2021) 107094, doi:10.1016/j.elecom.2021.107094.

[5] Z. Zhang, X. Feng, Z. Zhang, L. Chen, W. Liu, L. Tong, X. Gao, J. Zhang, Graphdiyne enabled nitrogen vacancy formation in copper nitride for efficient ammonia synthesis, J. Am. Chem. Soc. 146 (2024) 14898–14904, doi:10.1021/jacs.4c04985.

[6] W. Qiu, X. Chen, Y. Liu, D. Xiao, P. Wang, R. Li, K. Liu, Z. Jin, P. Li, Confining intermediates within a catalytic nanoreactor facilitates nitrate-to-ammonia electrosynthesis, Appl. Catal. B: Environ. 315 (2022) 121548, doi:10.1016/j.apcatb.2022.121548.

[7] R. Zhang, C. Li, H. Cui, Y. Wang, S. Zhang, P. Li, Y. Hou, Y. Guo, G. Liang, Z. Huang, C. Peng, C. Zhi, Electrochemical nitrate reduction in acid enables high-efficiency ammonia synthesis and high-voltage pollutes-based fuel cells, Nat. Commun. 14 (2023) 8036, doi:10.1038/s41467-023-43897-6.

[8] Y. Zheng, Y. Jiao, A. Vasileff, S. Qiao, The hydrogen evolution reaction in alkaline solution: From theory, single crystal models, to practical electrocatalysts, Angew. Chem. Int. Ed. 57 (2018) 7568–7579, doi:10.1002/anie.201710556.

[9] P. Zhao, H. Jiang, H. Shen, S. Yang, R. Gao, Y. Guo, Q. Zhang, H. Zhang, Construction of low-coordination Cu-C_2 single-atoms electrocatalyst facilitating the efficient electrochemical CO_2 reduction to methane, Angew. Chem. Int. Ed. 62 (2023) e202314121, doi:10.1002/anie.202314121.

[10] M. Xie, S. Tang, Z. Li, M. Wang, Z. Jin, P. Li, X. Zhan, H. Zhou, G. Yu, Intermetallic single-atom alloy In-Pd bimetallene for neutral electrosynthesis of ammonia from nitrate, J. Am. Chem. Soc. 145 (2023) 13957–13967, doi:10.1021/jacs.3c03432.

[11] Q. Gao, B. Yao, H.S. Pillai, W. Zang, X. Han, Y. Liu, S. Yu, Z. Yan, B. Min, S. Zhang, H. Zhou, L. Ma, H. Xin, Q. He, H. Zhu, Synthesis of core/shell nanocrystals with ordered intermetallic single-atom alloy layers for nitrate electroreduction to ammonia, Nat. Synth. 2 (2023) 624–634, doi:10.1038/s44160-023-00258-x.

[12] H. Zou, D. Cheng, C. Tang, W. Luo, H. Xiong, H. Dong, F. Li, T. Song, S. Shu, H. Dai, Z. Cui, Z. Lu, L. Duan, Electronic perturbation of Cu nanowire surfaces with functionalized graphdiyne for enhanced CO_2 reduction reaction, Natl. Sci. Rev. 11 (2024) nwae253, doi:10.1093/nsr/nwae253.

[13] L. Wu, L. Zhang, S. Liu, J. Feng, L. Xu, X. Tan, X. Ma, X. Sun, Promoting ambient ammonia electrosynthesis on modulated $Cu^{\delta+}$ catalysts by B-doping, J. Mater. Chem. A 11 (2023) 5520–5526, doi:10.1039/d3ta00227f.

[14] W. Jung, J. Jeong, Y. Chae, W.H. Lee, Y. Ko, K.H. Chae, H. Oh, U. Lee, D.K. Lee, B.K. Min, H. Shin, Y.J. Hwang, D.H. Won, Synergistic bimetallic CuPd oxide alloy electrocatalyst for ammonia production from the electrochemical nitrate reaction, J. Mater. Chem. A 10 (2022) 23760–23769, doi:10.1039/d2ta06316f.

[15] L. Sun, C. Dai, T. Wang, X. Jin, Z.J. Xu, X. Wang, Modulating the electronic structure of cobalt in molecular catalysts via coordination environment regulation for highly efficient heterogeneous nitrate reduction, Angew. Chem. Int. Ed. 63 (2024) e202320027, doi:10.1002/anie.202320027.

[16] S. Shu, T. Song, C. Wang, H. Dai, L. Duan, [2+1] cycloadditions modulate the hydrophobicity of Ni-N_4 single-atom catalysts for efficient CO_2 electroreduction, Angew. Chem. Int. Ed. 63 (2024) e202405650, doi:10.1002/anie.202405650.

[17] X.F. Yang, A. Wang, B. Qiao, J. Li, J. Liu, T. Zhang, Single-atom catalysts: A new frontier in heterogeneous catalysis, Acc. Chem. Res. 46 (2013) 1740–1748, doi:10.1021/ar300361m.

[18] H. Zou, L.J. Arachchige, W. Rong, C. Tang, R. Wang, S. Tan, H. Chen, D. He, J. Hu, E. Hu, C. Sun, L. Duan, Low-valence metal single atoms on graphdiyne promotes electrochemical nitrogen reduction via M-to-N_2 π-backdonation, Adv. Funct. Mater. 32 (2022) 2200333, doi:10.1002/adfm.202200333.

[19] Z. Wu, M. Karamad, X. Yong, Q. Huang, D.A. Cullen, P. Zhu, C. Xia, Q. Xiao, M. Shakouri, F. Chen, J.Y.T. Kim, Y. Xia, K. Heck, Y. Hu, M. Wong, Q. Li, I. Gates, S. Siahrostami, H. Wang, Electrochemical ammonia synthesis via nitrate reduction on Fe single atom catalyst, Nat. Commun. 12 (2021) 2870, doi:10.1038/s41467-021-23115-x.

[20] Y. Wang, H. Yin, F. Dong, X. Zhao, Y. Qu, L. Wang, Y. Peng, D. Wang, W. Fang, J. Li, N-coordinated Cu–Ni dual-single-atom catalyst for highly selective electrocatalytic reduction of nitrate to ammonia, Small 19 (2023) 2207695, doi:10.1002/smll.202207695.

[21] J. Xu, S. Zhang, H. Liu, S. Liu, Y. Yuan, Y. Meng, M. Wang, C. Shen, Q. Peng, J. Chen, X. Wang, L. Song, K. Li, W. Chen, Breaking local charge symmetry of iron single atoms for efficient electrocatalytic nitrate reduction to ammonia, Angew. Chem. Int. Ed. 62 (2023) e202308044, doi:10.1002/anie.202308044.

[22] Y. Zhou, L. Zhang, Z. Zhu, M. Wang, N. Li, T. Qian, C. Yan, J. Lu, Optimizing intermediate adsorption over PdM (M = Fe, Co, Ni, Cu) bimetallene for boosted nitrate electroreduction to ammonia, Angew. Chem. Int. Ed 63 (2024) e202319029, doi:10.1002/anie.202319029.

[23] W. Liao, J. Wang, G. Ni, K. Liu, C. Liu, S. Chen, Q. Wang, Y. Chen, T. Luo, X. Wang, Y. Wang, W. Li, T.S. Chan, C. Ma, H. Li, Y. Liang, W. Liu, J. Fu, B. Xi, M. Liu, Sustainable conversion of alkaline nitrate to ammonia at activities greater than 2 A cm^{-2}, Nat. Commun. 15 (2024) 1264, doi:10.1038/s41467-024-45534-2.

[24] J. Lim, C. Liu, J. Park, Y. Liu, T.P. Senftle, S.W. Lee, M.C. Hatzell, Structure sensitivity of Pd facets for enhanced electrochemical nitrate reduction to ammonia, ACS Catal. 11 (2021) 7568–7577, doi:10.1021/acscatal.1c01413.

[25] J. Martínez, A. Ortiz, I. Ortiz, State-of-the-art and perspectives of the catalytic and electrocatalytic reduction of aqueous nitrates, Appl. Catal. B: Environ. 207 (2017) 42–59, doi:10.1016/j.apcatb.2017.02.016.

[26] X. Wu, M. Nazemi, S. Gupta, A. Chismar, K. Hong, H. Jacobs, W. Zhang, K. Rigby, T. Hedtke, Q. Wang, E. Stavitski, M.S. Wong, C. Muhich, J.H. Kim, Contrasting capability of single atom palladium for thermocatalytic versus electrocatalytic nitrate reduction reaction, ACS Catal. 13 (2023) 6804–6812, doi:10.1021/acscatal.3c01285.

[27] C. Du, S. Lu, J. Wang, X. Wang, M. Wang, H.M. Fruehwald, L. Wang, B. Zhang, T. Guo, J.P. Mills, W. Wei, Z. Chen, Y. Teng, J. Zhang, C. Sun, H. Zhou, R.D.L. Smith, B. Kendall, G. Henkelman, Y. Wu, Selectively reducing nitrate into NH_3 in neutral media by PdCu single-atom alloy electrocatalysis, ACS Catal. 13 (2023) 10560–10569, doi:10.1021/acscatal.3c01088.

[28] G. Li, Y. Li, H. Liu, Y. Guo, Y. Li, D. Zhu, Architecture of graphdiyne nanoscale films, Chem. Comm. 46 (2010) 3256–3258, doi:10.1039/b922733d.

[29] T. Song, H. Liu, H. Zou, C. Wang, S. Shu, H. Dai, L. Duan, Metal-free wet chemistry for the fast gram-scale synthesis of gamma-graphyne and its derivatives, Angew. Chem. Int. Ed. 63 (2024) e202411228, doi:10.1002/anie.202411228.

[30] W. Rong, H. Zou, S. Tan, E. Hu, F. Li, C. Tang, H. Dai, S. Wei, Y. Ji, L. Duan, Few-atom copper catalyst for the electrochemical reduction of CO to acetate: Synergetic catalysis between neighboring Cu atoms, CCS Chem 5 (2023) 1176–1188, doi:10.31635/ccschem.022.202201910.

[31] W. Rong, H. Zou, W. Zang, S. Xi, S. Wei, B. Long, J. Hu, Y. Ji, L. Duan, Size-dependent activity and selectivity of atomic-level copper nanoclusters during CO/CO_2 electroreduction, Angew. Chem. Int. Ed. 60 (2021) 466–472, doi:10.1002/anie.202011836.

[32] H. Liu, H. Zou, D. Wang, C. Wang, F. Li, H. Dai, T. Song, M. Wang, Y. Ji, L. Duan, Second sphere effects promote formic acid dehydrogenation by a single-atom gold catalyst supported on amino-substituted graphdiyne, Angew. Chem. Int. Ed. 62 (2023) e202216739, doi:10.1002/anie.202216739.

[33] J. Li, L. Zhong, L. Tong, Y. Yu, Q. Liu, S. Zhang, C. Yin, L. Qiao, S. Li, R. Si, J. Zhang, Atomic Pd on graphdiyne/graphene heterostructure as efficient catalyst for aromatic nitroreduction, Adv. Funct. Mater. 29 (2019) 1905423, doi:10.1002/adfm.201905423.

[34] D. Wang, L. Zhang, S. Chen, Q. Pan, Z. Yu, X. Jia, L. He, C. Li, Y. Zhao, Preparation of a large amount of ultrathin graphdiyne, Chem. Eur. J. 28 (2022) e2200442, doi:10.1002/chem.202200442.

[35] X. Yin, S. Tang, C. Zhang, H. Wang, R. Si, X. Lu, T. Lu, Graphdiyne-based Pd single-atom catalyst for semihydrogenation of alkynes to alkenes with high selectivity and conversion under mild conditions, J. Mater. Chem. A 8 (2020) 20925–20930, doi:10.1039/d0ta07705d.

[36] H. Zou, G. Zhao, H. Dai, H. Dong, W. Luo, L. Wang, Z. Lu, Y. Luo, G. Zhang, L. Duan, Electronic perturbation of copper single-atom CO_2 reduction catalysts in a molecular way, Angew. Chem. Int. Ed. 62 (2022) e202217220, doi:10.1002/anie.202217220.

[37] E.A. Moges, C. Chang, W. Huang, K. Lakshmanan, Y.A. Awoke, C. Pao, M. Tsai, W. Su, B.J. Hwang, Sustainable synthesis of dual single-atom catalyst of Pd-N_4/Cu-N_4 for partial oxidation of ethylene glycol, Adv. Funct. Mater. 32 (2022) 2206887, doi:10.1002/adfm.202206887.

[38] R. Bai, G. He, J. Li, L. Li, T. Zhang, X. Wang, W. Zhang, Y. Zou, J. Zhang, D. Mei, A. Corma, J. Yu, Heteroatoms-stabilized single palladium atoms on amorphous zeolites: Breaking the tradeoff between catalytic activity and selectivity for alkyne semihydrogenation, Angew. Chem. Int. Ed. 63 (2024) e202410017, doi:10.1002/anie.202410017.

[39] Z. Huang, B. Yang, Y. Zhou, W. Luo, G. Chen, M. Liu, X. Liu, R. Ma, N. Zhang, Tungsten nitride/tungsten oxide nanosheets for enhanced oxynitride intermediate adsorption and hydrogenation in nitrate electroreduction to ammonia, ACS Nano 17 (2023) 25091–25100, doi:10.1021/acsnano.3c07734.

[40] G. Zhang, G. Wang, Y. Wan, X. Liu, K. Chu, Ampere-level nitrate electroreduction to ammonia over monodispersed Bi-doped FeS_2, ACS Nano 17 (2023) 21328–21336, doi:10.1021/acsnano.3c05946.

[41] W. Tang, E. Sanville, G. Henkelman, A grid-based bader analysis algorithm without lattice bias, J. Phys. Condens. Matter. 21 (2009) 084204, doi:10.1088/0953-8984/21/8/084204.

[42] R. Warburton, A. Soudackov, S. Hammes-Schiffer, Theoretical modeling of electrochemical proton-coupled electron transfer, Chem. Rev. 122 (2022) 10599–10650, doi:10.1021/acs.chemrev.1c00929.

[43] W. Ran, H. Zhao, X. Zhang, S. Li, J. Sun, J. Liu, R. Liu, G. Jiang, Critical review of Pd-catalyzed reduction process for treatment of waterborne pollutants, Environ. Sci. Technol. 58 (2024) 3079–3097, doi:10.1021/acs.est.3c09198.

[44] X. Cheng, J. He, H. Ji, H. Zhang, Q. Cao, W. Sun, C. Yan, J. Lu, Coordination symmetry breaking of single-atom catalysts for robust and efficient nitrate electroreduction to ammonia, Adv. Mater. 34 (2022) e2205767, doi:10.1002/adma.202205767.

[45] X. Min, B. Liu, Microenvironment engineering to promote selective ammonia electrosynthesis from nitrate over a PdCu hollow catalyst, Small 19 (2023) e2300794, doi:10.1002/smll.202300794.

[46] Z. Yu, T. Ren, J. Xie, H. Yu, K. Deng, Z. Wang, H. Wang, L. Wang, Y. Xu, Yttrium atomically incorporated into Co(OH)F nanowires enables efficient electrochemical reduction of nitrate to ammonia, Chem. Comm. 59 (2023) 13875–13878, doi:10.1039/d3cc03293k.

[47] Q. Song, M. Li, X. Hou, J. Li, Z. Dong, S. Zhang, L. Yang, X. Liu, Anchored Fe atoms for N=O bond activation to boost electrocatalytic nitrate reduction at low concentrations, Appl. Catal. B: Environ. 317 (2022) 121721, doi:10.1016/j.apcatb.2022.121721.

[48] F. Chen, Z. Wu, S. Gupta, D. Rivera, S. Lambeets, S. Pecaut, J. Kim, P. Zhu, Y. Finfrock, D. Meira, G. King, G. Gao, W. Xu, D. Cullen, H. Zhou, Y. Han, D. Perea, C. Muhich, H. Wang, Efficient conversion of low-concentration nitrate sources into ammonia on a Ru-dispersed Cu nanowire electrocatalyst, Nat. Nanotechnol. 17 (2022) 759–767, doi:10.1038/s41565-022-01121-4.

[49] Q. Wu, F. Zhu, G. Wallace, X. Yao, J. Chen, Electrocatalysis of nitrogen pollution: Transforming nitrogen waste into high-value chemicals, Chem. Soc. Rev. 53 (2024) 557–565, doi:10.1039/d3cs00714f.